In situ growth CNT@MOFs core-shell structures enabling high specific supercapacitances in neutral aqueous electrolyte

Mingxia Lu[1], Gang Wang[1] (✉), Xiping Yang[1], and Bo Hou[2] (✉)

[1] School of Chemistry and Chemical Engineering, Henan University of Technology, Zhengzhou 450001, P. R. China.

[2] Department of Physics and Astronomy, Cardiff University, Cardiff CF24 3AA, UK

* Corresponding author: Email: HouB6@cardiff.ac.uk (Bo Hou)

** Corresponding author: Email: gwang198@gmail.com (Gang Wang)

ABSTRACT

Conductive metal-organic frameworks (c-MOFs) are promising active electrode materials for electrochemical double-layer capacitors with a performance that already exceeds most carbon-based materials. However, their excellent supercapacitance is primarily based on organic or alkaline electrolytes, which largely impede their broad applications and sustainabilities. In this work, we propose a new synthesis approach for fabricating carbon nanotubes (CNTs) and c-MOF core-shell structures (CNT@MOFs), which result in high supercapacitance in neutral aqueous electrolytes. We identify that CNTs provide abundant active sites to ensure high capacitance, and $Ni_3(HITP)_2$ nanoarrays that in-situ grow on the surface of CNTs bundles can significantly improve the conductivity and provide enough ion transport pathways in aqueous electrolyte. Specifically, using CNT@MOFs core-shell structures as an electrode, we obtained a high initial capacitance of 150.7 $F \cdot g^{-1}$ at 0.1 $A \cdot g^{-1}$ in 1 M Na_2SO_4 solution and good capacity retention of 83.5% after 10000 cycles at 4 $A \cdot g^{-1}$. We also found that the carboxyl groups on the surface of CNTs provide better anchor sites for the in situ growth of c-MOF, which promotes the uniform growth of c-MOF shells on the CNT surface and improves aqueous electrolyte accessibility. We believe that the high supercapacitance in aqueous electrolytes reported in this work would provide a good prospect for deploying c-MOF based energy storage devices into biomedical and other healthcare electronic applications.

KEYWORDS

Carbon nanotubes, metal-organic frameworks, conductive MOFs, supercapacitor, neutral aqueous electrolyte

1 Introduction

Metal-organic frameworks (MOFs), due to their tunable structure, rich micropore structure, and high specific surface area [1-3] have been widely researched and applied in many fields, such as supercapacitors [4, 5], batteries [6, 7], electrocatalysis [8, 9], sensors [10], drug delivery [11, 12], and recently reported airborne water harvest [13-15]. However, the poor electrical conductivity and stability of most traditional MOFs, in particular, their poor electrochemical performance in aqueous electrolytes, significantly limit their applications [16-18]. Generally, there are two strategies to address this challenge: i) developing new MOFs materials with high conductivity and stable structure [19], ii) composite with high conductive materials, such as graphene, carbon nanotubes (CNTs), conductive polymers [20, 21].

So far, the most challenging and potentially rewarding approach is to synthesis new MOFs materials with high charge mobility and electrical conductivity. Since the discovery of $Cu[Cu(pdt)_2]$ (conductivity: 1×10^{-2} $S\cdot m^{-1}$) in 2009 by Takaishi [22], nearly 20 types of conductive MOFs (c-MOFs) were designed and synthesised, such as $M(C_2H_2N_3)_2$ (M = Mg, Mn, Fe, Co, Cu, Zn) [23], $Cu_3(BTC)_2$ [24], $M_2(DXBDC)$ (M = Mg, Fe, X = O, S) [25, 26], $M_2(TTFTB)$ (M = Mn, Co, Zn, Cd) [27], $M_3(HXTP)_2$ (M = Co, Ni, Cu, Pt, X = O, S, NH) [4, 28-31], M-HAB (M = Co, Ni, Cu) [32], $M_3(HHTT)_2$ (M = Ni, Cu) [33]. Among them, 2D c-MOFs have shown the highest conductivity values, most likely due to the in-plane charge delocalization and extended π-conjugation in the 2D sheets [34]. Sheberla and co-workers have reported a 2D c-MOF $Ni_3(HITP)_2$ (HITP = 2,3,6,7,10,11-hexaiminotriphenylene), which has a bulk (pellet) conductivity value of 200 $S\cdot m^{-1}$ [35]. As the electrode of the supercapacitor, $Ni_3(HITP)_2$ exhibited a capacitance of 102 $F\cdot g^{-1}$ at 0.1 $A\cdot g^{-1}$ and remained 90% after 10000 cycles in 1 M $TEABF_4$/CAN electrolyte. $M_3(HXTP)_2$, $M_3(HHTT)_2$, and M-HAB are π-stacked

2D c-MOFs with an extended π-conjugate plane structure, similar to graphite. The high conductivity of 2D c-MOFs originates from their extended π-conjugate structure, giving it more π-π and π-d orbital overlap, while π-π stacking between layers also enables spatial charge transfer [36, 37]. However, further improving the capacitance and energy density is challenging. Currently, adding electrochemically active materials as additives and composite materials into c-MOF is well acknowledged as an efficient approach. For example, assembling MOFs with high conductive carbon materials such as graphene, CNTs, carbon black, and so on has become an effective strategy for improving energy storage efficiency [21, 38, 39].

Among these materials, CNTs exhibit high electrical conductivity, large surface area, and excellent cycle life, which enable them to be the most promising conductive composites materials [40]. For example, Wen and co-workers synthesized Ni-MOF/CNT composites, which exhibited good electrochemical activity due to the synergism between the specific structure of pristine Ni-MOF and the high conductivity of CNTs, achieving a high specific capacitance of 1765 $F \cdot g^{-1}$ at 0.5 $A \cdot g^{-1}$ [21]. Ansari and co-workers synthesized Cu-MOF/CNT hybrids for supercapacitor applications reveal a high specific capacitance of 380 $F \cdot g^{-1}$ at 1.6 $A \cdot g^{-1}$ with a good rate performance [41].

More importantly, these results suggest that the introduction of conductive CNTs into porous MOFs structures not only enhanced the mechanical strength and conductivity but also enhanced the electrolyte accessibility throughout the charge-discharge process [18, 42, 43]. For instance, it was reported that the high conductivity of CNTs can improve the electron transport from the active material to the collector [21, 41]. Therefore, introducing conductive CNTs into porous MOFs structures is a feasible strategy for exploring the possibility of MOFs supercapacitance electrochemical energy storage in neutral aqueous electrolytes. Neutral aqueous electrolytes have the advantages of safety, simple manufacturing, low cost and environmental friendliness. More importantly, the ionic conductivity of aqueous electrolytes is usually much higher

than that of organic electrolytes, which leads to better rate performance.

Herein, a CNT@c-MOF core-shell structure was synthesized by the "bottom-up" approach which directly grew $Ni_3(HITP)_2$ (c-MOF) on the CNTs surface. A benchmark symmetric supercapacitor configuration was employed for evaluating the electrochemical supercapacitive performance of CNT@c-MOF in neutral aqueous electrolytes. Furthermore, different amounts of CNTs were tested to explore the effect of CNTs loading on the final morphological of CNT@c-MOF composites and their electrochemical energy storage performance. We found that the carboxyl groups on the surface of CNTs provide better anchor sites for the in situ growth of c-MOF, which promotes the uniform growth of c-MOF shells on the CNTs surface and improves aqueous electrolyte accessibility. However, the MOF/CNT-0.5 with CNTs content of 13.09 wt.% shows the best specific capacitance, rate performance, and cyclic durability.

2 Experimental section

2.1 Materials

Nickel chloride hexahydrate ($NiCl_2 \cdot 6H_2O$) and aqueous ammonium were purchased from Tianjin Fengchuan Chemical Reagent Technologies Co., Ltd (China). 2, 3, 6, 7, 10, 11-hexaaminotriphenylene hexahydrochloride (HATP·6HCl) was purchased from Zhengzhou Alfa Chemical Co., Ltd (China). The above chemicals were used directly without further purification. Single-walled carbon nanotubes (SWCNTs, purity >95%, external diameter <2 nm, length 0.3−5 μm) purchased from Aladdin Industrial Corporation were used after oxidation treatment by the mixture of H_2SO_4 and HNO_3 (3:1 v/v). Specific methods can refer to our previously published works [38, 44].

2.2 Synthesis of $Ni_3(HITP)_2$ powder

$Ni_3(HITP)_2$ was synthesized by mixing HATP·6HCl to $NiCl_2 \cdot 6H_2O$ following the procedure reported by Sheberla and co-workers [35]. Typically, the 40 mg of HATP·6HCl was dissolved in 20 mL of deionized water under continuous ultrasonication for 30 min and then transferred into a 100 mL flask. Meanwhile, the

26.4 mg of $NiCl_2 \cdot 6H_2O$ was dissolved in 20 mL of deionized water, added 1.2 mL $NH_3 \cdot H_2O$ (28%) and transferred to a 25 mL constant pressure drop funnel. After that, the $NiCl_2 \cdot 6H_2O$ solution was dropwise added into the flask under stirring and control the dropping speed is 1 drop/2 s. This mixture was stirred in a flask for 2 hours at 65 °C. The resulting black powder was filtered by a microporous membrane (0.22 μm), and washed with a large amount of water and acetone, and dried at 80℃ overnight. The final collected black powder was named c-MOF.

2.3 Synthesis of CNTs@$Ni_3(HITP)_2$ Powder

The preparation of CNTs@$Ni_3(HITP)_2$ composites followed the same procedures as that of $Ni_3(HITP)_2$ powder, except that the HATP·6HCl (40 mg) was dissolved in 20 mL of CNTs aqueous solution instead of deionized water. Typically, a series of CNTs dispersions with a concentration of 0.2, 0.5, and 1.0 $mg \cdot mL^{-1}$ was prepared by dispersing CNTs powder into deionized water under continuous ultrasonication (KQ-300VDE, 45 kHz, 8 h). After that, HATP·6HCl (40 mg) was dissolved in CNTs aqueous solution with further 30 min ultrasonication. Then, the preparation of CNTs@$Ni_3(HITP)_2$ hybrids followed the same procedures as that of $Ni_3(HITP)_2$ powder. For the different amounts of CNTs loading, each CNTs@$Ni_3(HITP)_2$ hybrid was denoted as c-MOF/CNT-0.2, c-MOF/CNT-0.5 and c-MOF/CNT-1.0, with CNTs concentration of 0.2, 0.5, and 1.0 $mg \cdot mL^{-1}$, respectively.

2.4 Characterization

The morphology was carried out by field emission scanning electron microscope (FESEM, Zeiss Sigma 300, Germany) with 10 kV operating voltage. High-resolution transmission electron microscopy (HRTEM) images were acquired using Titan G260-300 microscopy (FEI, USA). Fourier transform infrared spectroscopy was employed to identify the functional groups on the materials by a Nicolet Avatar 360 FT-IR spectrometer (FT-IR, Instrument Co., Madison, WI, USA). Raman spectra were collected on a LabRAM HR Evolution spectroscopy with an excitation wavelength of 532 nm (HORIBA Jobin Yvon, France). X-ray diffraction (XRD) patterns were

recorded using a Rigaku MiniFlex 600 X-ray diffractometer (Rigaku Co., Tokyo, Japan) with Cu Kα radiation over the 2θ range of 3-80°. X-ray photoelectron spectroscopy (XPS) was performed on a Thermo Scientific K-alpha instrument (Thermo Scientific Inc. USA). The N_2 adsorption isotherms were measured by a Micromeritics ASAP 2460 gas sorption analyzer (Micromeritics Instrument Corp., USA) at 77 K. The electrical conductivity was performed on an RTS-9 (4 PROBES TECH, Guangzhou, China) four-point probes station.

2.5 Electrochemical Measurements

The working electrode was prepared by casting the slurry of 80 wt% active materials (c-MOF, or CNTs@$Ni_3(HITP)_2$ with different amounts of CNTs loading), 10 wt% conductive agents (carbon black), and 10 wt% binders (polyvinylidene fluoride, PVDF) in N-methyl-2-pyrrolidone (NMP) on the nickel foam current collector (1×1 cm^2) and dried at 80 ℃ for 12 h, and then pressed at a pressure of 10 MPa. The active materials loading of each electrode was 8 $mg \cdot cm^2$.

A CHI660E electrochemical workstation (Shanghai Chen Hua Instruments Co., Shanghai, China) was employed to test the electrochemical properties of all electrodes. All of the tests were carried out in a three-electrode cell consisting of the as-prepared electrode (1 cm × 2 cm) as the working electrode, a 2 cm × 2 cm Pt sheet as the counter electrode, Ag/AgCl (saturated KCl) as the reference electrode, and 1 M Na_2SO_4 aqueous solution as the electrolyte. Cyclic voltammogram (CV) curves were tested at various scan rates of 5, 10, 20, 40, 60, 80, and 100 $mV \cdot s^{-1}$ with a potential window of -0.2-0.4 V. Electrochemical impedance spectroscopy (EIS) measurements were performed in a frequency range from 10^{-2} to 10^5 Hz with an ac amplitude of 5 mV at open circuit potential. Galvanostatic charge−discharge (GCD) tests were carried out at a current of 0.1, 0.2, 0.4, 0.6, 0.8, 1.0, 2.0, 3.0, 4.0, 5.0, and 6.0 $A \cdot g^{-1}$ with a cutoff voltage of -0.2-0.4 V.

The gravimetric specific capacitance (Cs) was calculated from the GCD discharge

curves using the following equation:

$$Cs\ (F\cdot g^{-1}) = \int I(U)\ dU/(2\cdot m\cdot \upsilon\cdot \Delta U) \qquad (1)$$

$$\text{and } Cs\ (F\cdot g^{-1}) = I\cdot \Delta t/(m\cdot \Delta U) \qquad (2)$$

where I is the discharging current (A), Δt is the discharging time (s), m is the mass of active material on one electrode (g), and ΔU (V) is the potential discharging range.

The symmetric supercapacitor (SC) was fabricated with a 1.0 M Na_2SO_4 aqueous solution to evaluate the energy density. Two GCA 2-2 electrodes were immersed in 1.0 M Na_2SO_4 aqueous solution for 12 h and then separated by filter paper soaked with electrolyte. The GCD test was performed at a current density of 1 $A\cdot g^{-1}$ with a potential range of -0.2-0.4 V.

The gravimetric specific capacitance (Cs) was calculated based on the total mass of two electrodes:

$$Cs\ (F\cdot g^{-1}) = 4I\cdot \Delta t/(m\cdot \Delta U) \qquad (2)$$

$$\text{and } Cs\ (F\cdot g^{-1}) = \int I(U)\ dU/(2\cdot m\cdot \upsilon\cdot \Delta U) \qquad (3)$$

where υ is the scan rate ($V\cdot s^{-1}$).

3 Results and discussion

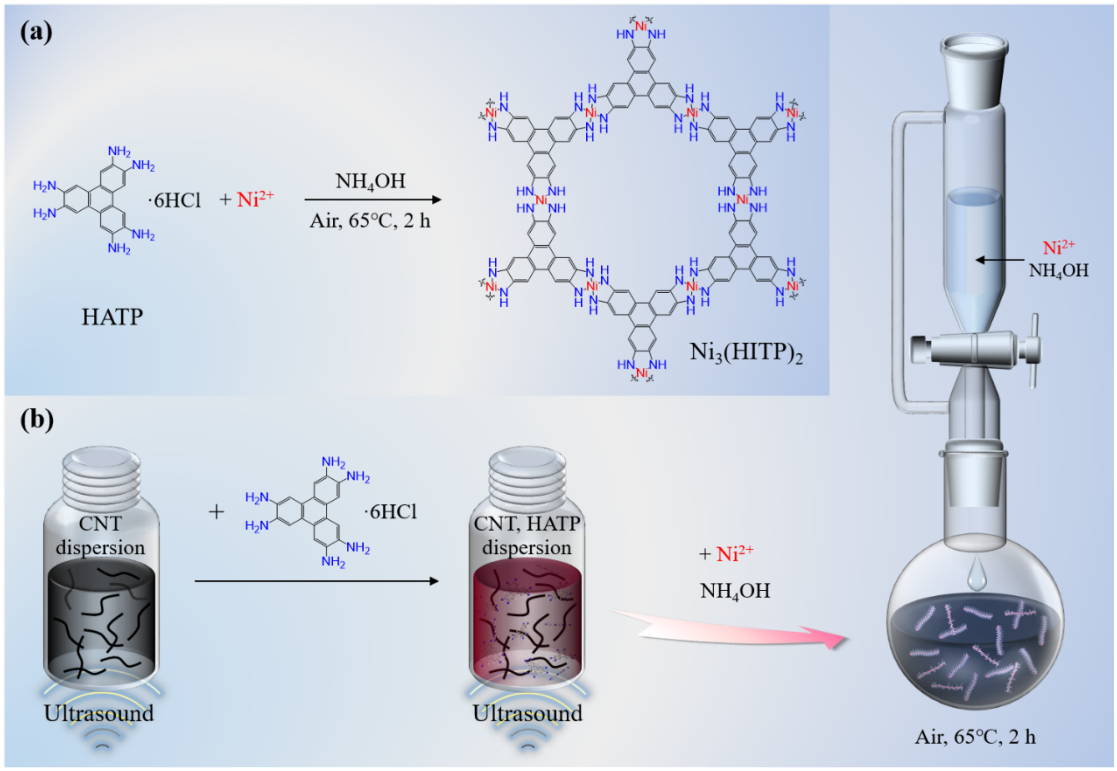

Figure 1. Schematic diagrams of (a) the synthesis of $Ni_3(HITP)_2$ (named c-MOF), and (b) the synthesis of $Ni_3(HITP)_2$/CNTs (named c-MOF/CNT).

The fabrication processes of $Ni_3(HITP)_2$ and c-MOF/CNT composites are schematically shown in Figure 1a-b. $Ni_3(HITP)_2$ powder was prepared via the chemical reaction between HATP·6HCl and $NiCl_2·6H_2O$ in NH_4OH at 65 °C. After being filtered, rinsed, and dried, a black powder of $Ni_3(HITP)_2$ was obtained. It features a two-dimensional (2D) hexagonal lattice structure by coordinating Ni ions and HATP ligands in a long-range order with the AB stacking arrangement within the *ab* plane. Compared with traditional MOFs, the high conductivity of c-MOF originates from their own extended π-conjugate structure, which offers it a more π-π and π-d orbital overlap. In addition, π-π stacking between layers also enables spatial charge transfer. The effective orbital overlaps between Ni ions and organic HATP ligands contribute a high conductivity over 500 $S·m^{-1}$ (Figure S1), exceeding those of the activated carbon [45]. The preparation process of c-MOF/CNT composites is shown in Figure 1b. First, HATP·6HCl was physisorption in CNTs dispersion with 30 min ultrasonication, and then transferred into a flask. HATP·6HCl molecules are then physisorption to the

surface of CNTs via π-π interaction. Meanwhile, the mixed aqueous solution of $NiCl_2 \cdot 6H_2O$ and $NH_3 \cdot H_2O$ (28%) was set in a 25 mL constant pressure drop funnel. After that, the Ni^{2+} solution was dropwise added into the flask. This mixture was stirred in a flask for 2 hours at 65 °C. At this stage, the c-MOF shelling layer was formed.

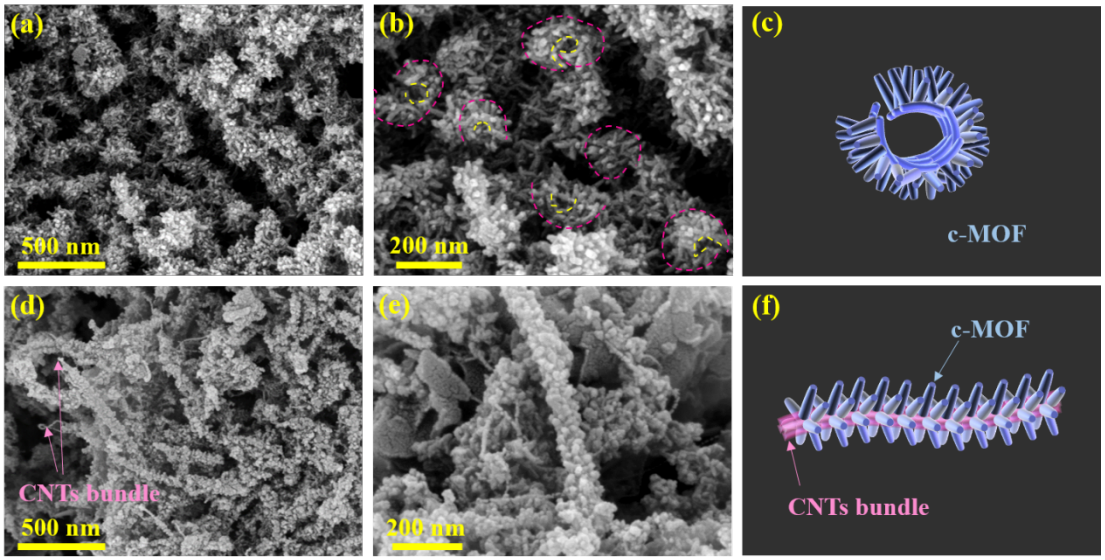

Figure 2. The SEM of (a, b) $Ni_3(HITP)_2$, and (d, e) c-MOF/CNT-0.5.

The morphological structures of $Ni_3(HITP)_2$ and c-MOF/CNT are characterized at different scales through SEM analysis. Figure 2a-b shows the structure and morphology of $Ni_3(HITP)_2$. The finger-like structure is composed of a stacking layered $Ni_3(HITP)_2$ nanosheet with a width of about 10-20 nm and a length of 100-200 nm. The finger-like structure is self-assembled again to form nanoarrays, and then scrolled to form a ring structure (Figure 2c shows the model of structure). This structure is further demonstrated in the following TEM analysis. As shown in Figure S2b, the internal diameter of the "ring" is about 50-100 nm and the external diameter is about 100-200 nm. The structure of $Ni_3(HITP)_2$ is a two-dimensional in-plane π-conjugated material. In $Ni_3(HITP)_2$, Ni atom adopts dsp^2 hybridization, forming a 2D conjugation. Their morphology was further confirmed by transmission electron microscopy (Figure 3 and Figure S3).

As shown in Figure 2c-d, the SEM picture of c-MOF/CNT-0.5 shows a large of

uniformly growing nanoarrays on the nanotube bundles, indicating that $Ni_3(HITP)_2$ has successfully assembled on the CNTs surface. However, the presence of particles is rarely observed on the more thin CNTs bundles, suggesting the difficulty of composites on the nanotubes with a smaller radius of curvature. The structure model of the c-MOF/CNT composite is shown in Figure 2f. Meanwhile, the c-MOF can be evenly loaded onto the CNTs bundles. When CNTs are overloaded, few nanoarrays can be observed.

The SEM images of c-MOF/CNT composites with different CNTs contents are shown in Figure S4. Because of the difficulties of dispersing CNTs powder into deionized water, CNTs usually tend to be stacked together to form bundles. In Figure S3, we can observe that the diameter of the bundle increases with the increasing CNTs content.

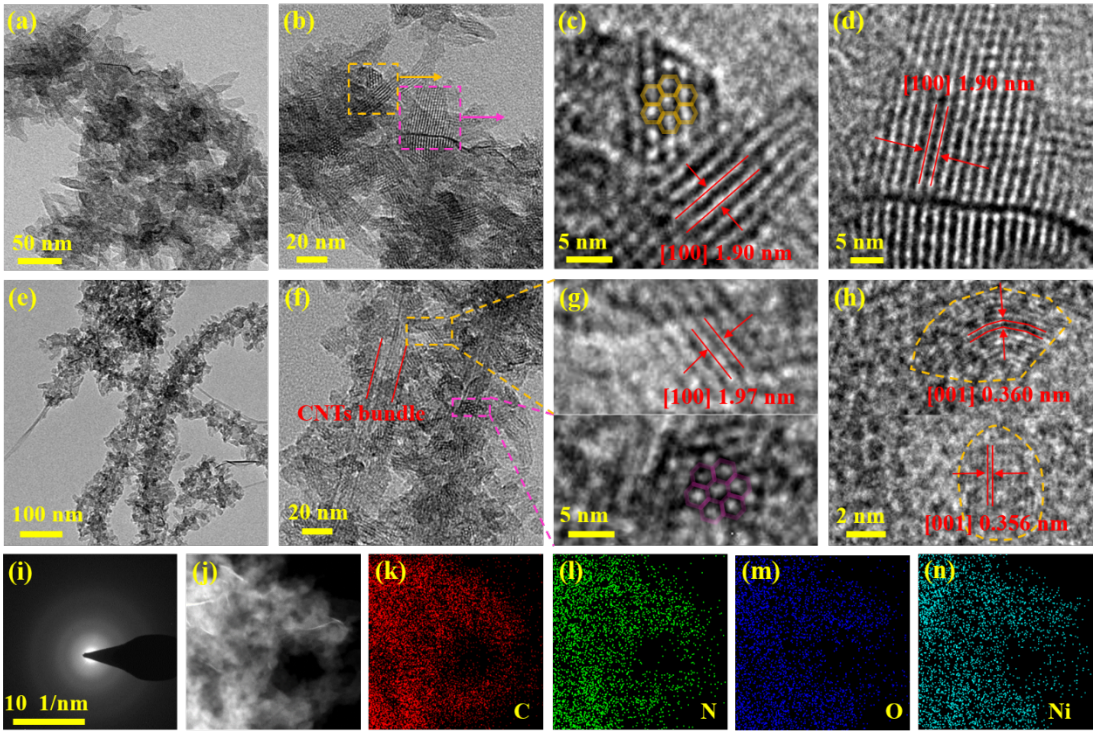

Figure 3. The TEM images of (a-d) $Ni_3(HITP)_2$, and (e-h) c-MOF/CNT-0.5. (i) SAED pattern of c-MOF/CNT-0.5. (j) EDS elemental mapping of c-MOF/CNT-0.5 with (k) C, (l) N, (m) O, and (n) Ni elements from a selected area.

Based on the SEM analysis, we propose that the c-MOF molecules are coupled via

weak metal-metal interaction and strongly bonded on the CNTs surface by way of π-π conjugation. To verify our hypothesis, the detailed morphological features of $Ni_3(HITP)_2$ and c-MOF/CNT-0.5 (CNT@c-MOF with CNT concentration of 0.5 $mg \cdot mL^{-1}$) composite are investigated by high-resolution TEM (HRTEM). The morphological structure of $Ni_3(HITP)_2$ shown in Figures 3a and b is consistent with the SEM results. As shown in Figures 3c and d, $Ni_3(HITP)_2$ presents clear hexagonal lattices of 1.90 nm indicates parallel 1D pores, consistent with the periodic arrangement of hexaiminotriphenylenes linked by the square planar metal centers. The crystalline nature of CNTs bundles and $Ni_3(HITP)_2$ can be easily recognized from the HRTEM image of the c-MOF/CNT-0.5 composite (Figure 3c and d). HRTEM image of c-MOF/CNT-0.5 composite (Figure 3g) showed that the $Ni_3(HITP)_2$ bonded on the CNTs surface also presents clear hexagonal lattices of 1.97 nm. The π–π stacking distance of the c-MOF/CNT-0.5 composite is measured as 0.36 nm (Figure 3h), which is consistent with the d-spacing between the crystalline (001) plane of $Ni_3(HITP)_2$ [46]. The selected area electron diffraction (SAED) pattern (Figure 3i) showing diffused ring patterns indicates poor crystallinity. Selected area TEM elemental mapping (Figure 3j) was employed to further confirm the uniform distribution of the c-MOF/CNT-0.5 composite. As depicted in Figure 3k-n, the characteristic elements for c-MOF/CNT-0.5, including C, N, O, and Ni, are evenly distributed on the surface of the c-MOF/CNT-0.5.

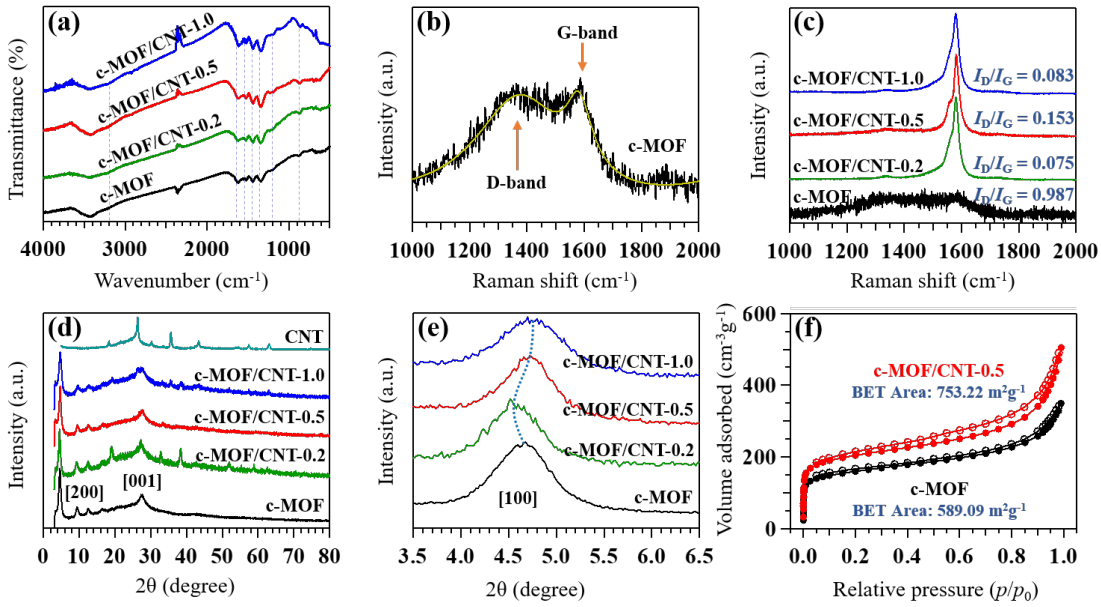

Figure 4. (a) FTIR spectra, (b, c) Raman spectra, (d, e) XRD patterns of c-MOF, c-MOF/CNT-0.2, c-MOF/CNT-0.5, and c-MOF/CNT-1.0. (f) N_2 adsorption/desorption isotherms of c-MOF and c-MOF/CNT-0.5.

FTIR analysis was carried out to investigate the chemical structure of c-MOF and c-MOF/CNT powder with different CNTs contents. As shown in Figure 4a, the absorption peak at 3430 cm^{-1} belonging to N-H stretching vibration on $Ni_3(HITP)_2$ or O-H hydroxyl stretching vibration of adsorbed water. The peak located at 1620 cm^{-1} is caused by C=C benzene skeleton vibration. The signals observed at 1520 and 1340 cm^{-1} represent the antisymmetric stretching vibration and symmetrical stretching vibration of $–NO_2$, which indicates that the partial ammonia groups are oxidized. The other peaks, such as 1440, 1360~1020, and 900~650 cm^{-1} correspond to C-H in-plane bending vibration, C-N stretching vibration, and C-H or N-H out-of-plane bending vibration, respectively. The presence of N-H, C=C, C-N demonstrates the successful synthesis of $Ni_3(HITP)_2$. The similar absorption spectra of c-MOF and CNT@c-MOF with different CNTs loading ratios suggest that c-MOF is successfully assembled on the surface of CNTs rather than a simple mixing process.

In addition, Raman spectroscopy was employed to study the structural changes of c-MOF/CNT composite as a function of CNTs contents. As shown in Figure 4b and Figure S5, two peaks centered at 1580 cm^{-1} (G-band) and 1320 cm^{-1} (D-band) can be revealed, which are usually associated with the vibration of sp^2 hybrid carbon atoms and the defect or disorder structure, respectively. The peak intensity ratio of the D-band and G-band (I_D/I_G) of c-MOF is about 0.987, which is considerably higher than those of c-MOF/CNT-0.2 (0.075), c-MOF/CNT-0.5 (0.153), and c-MOF/CNT-1.0 (0.075), indicating the high disorder degree in sp^2 carbon (Figure 4c). Compared with other c-MOF/CNT composites, c-MOF/CNT-0.5 shows the highest I_D/I_G value, implying more defects or disorders can enable more active sites for energy storage.

To better understand the crystal structure changes of c-MOF/CNT composites as a

function of CNTs contents, the XRD analysis of c-MOF and c-MOF/CNT composites is performed and shown in Figure 4d. The prominent peaks at 2θ = 4.7°, 9.5°, 12.6°, 16.5°, and 27.3°, indicate the successful synthesis of $Ni_3(HITP)_2$ crystals. The diffraction peak at 2θ = 4.7° is attributed to the (100) crystal plane of $Ni_3(HITP)_2$ with an interlayer spacing of 2.09 nm. The weaker and broader peak at 2θ = 27.3° is attributed to the (001) crystal plane with an interlayer spacing of 0.36 nm, which is consistent with the TEM test results. Compared with $Ni_3(HITP)_2$, no significant changes are observed for the peak position and FWHM of these peaks in c-MOF/CNT composites, indicating that $Ni_3(HITP)_2$ is successfully assembled on the surface of CNTs. However, as the CNTs content increased, a slight displacement was observed (Figure 4e and Figure S6), which indicates that the addition of CNTs may alter the crystal structure of c-MOF via additional π-π stacking and interaction.

N_2 adsorption isotherms at 77 K and pore size distributions of c-MOF and c-MOF/CNT-0.5 are presented in Figure 4f and Figure S5. The Brunauer–Emmett–Teller (BET) specific surface areas of c-MOF and c-MOF/CNT-0.5 are determined to be 589.09 $m^2 \cdot g^{-1}$ and 753.22 $m^2 \cdot g^{-1}$, respectively (Table S1). The higher specific surface area of the c-MOF/CNT-0.5 indicates a higher micropore volume (Figure S7). The results were further confirmed with pore size distribution curves based on non-local density functional theory (DFT) calculation which is a typical method for extracting pore size distributions from nanoporous materials (Figure S6).[1] The curves show peaks centered at around 0.95 nm, which suggests the existence of microporous structure in c-MOF. Furthermore, the intensity of the centered differential pore volume peak of c-MOF/CNT-0.5 is higher than that of c-MOF, exhibiting an improvement of the microporous structure.

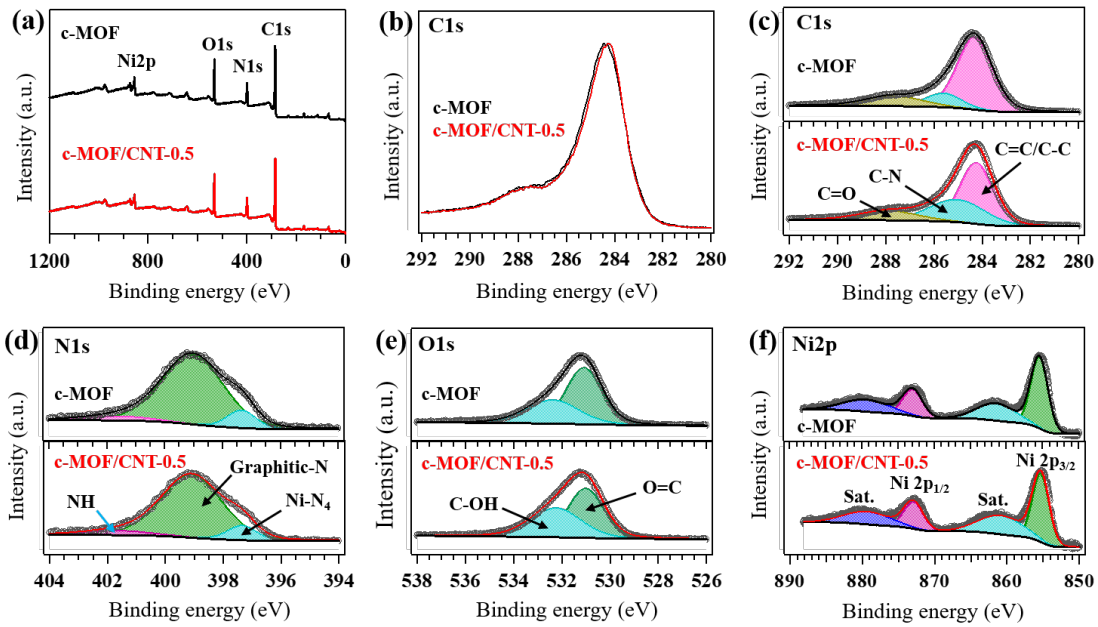

Figure 5. (a) Wide-scanned XPS spectra, and XPS core spectra corresponding to (b, c) C 1s, (d) N 1s, (e) O 1s, and (f) Ni 2p of c-MOF and c-MOF/CNT-0.5.

XPS measurements were carried out to investigate the chemical compositions and elemental oxidation state. From the wide-scanned XPS spectra shown in Figure 5a, the existence of Ni 2p, O 1s, N 1s, and C 1s resonance peaks can be observed. The contents of C, N, O, and Ni elements are 68.14%, 12.64%, 17.85%, and 1.37% for $Ni_3(HITP)_2$, and 70.42%, 11.49%, 16.95%, and 1.13% for c-MOF/CNT-0.5. The high O content is due to the partial oxidation of $Ni_3(HITP)_2$ during the synthesis process. The presence of CNTs reduced the content of O in the c-MOF/CNT-0.5 composite. The C 1s spectra were divided into three main peaks centered at 284.3, 285.6, and 287.7 eV for $Ni_3(HITP)_2$ and 284.3, 285.1, and 287.9 eV for c-MOF/CNT-0.5. These peaks are attributed to C=C/C-C, C-N, and C=O bonds, respectively (Figure 5c). As shown in Figure 5d, the N 1s spectra are mainly divided into three peaks with a binding energy of 397.4, 399.1, and 401.7 eV corresponding to N-Ni, graphitic-N, and N-H, respectively. The XPS spectra of O 1s were fitted with two prominent peaks are assigned to O=C and C-OH with binding energies of 531.1 and 282.3 eV, respectively (Figure 5e). Specifically, the Ni 2p spectra were fitted with four individual peaks, which are belonging to Ni $2p_{3/2}$, Ni $2p_{3/2}$ satellite, Ni $2p_{1/2}$, and Ni $2p_{1/2}$ satellite with binding

energies of 855.4, 861.7, 873.0, and 879.8 eV, respectively (Figure 5f), confirming that the oxidation state of Ni in $Ni_3(HITP)_2$ is +2. Compared with pristine $Ni_3(HITP)_2$, it is clear that the binding energy of Ni $2p_{3/2}$ and Ni $2p_{1/2}$ in c-MOF/CNT-0.5 is almost the same as those in $Ni_3(HITP)_2$. It indicates that there are no changes in the chemical composition or chemical environment of Ni in $Ni_3(HITP)_2$ after composing.

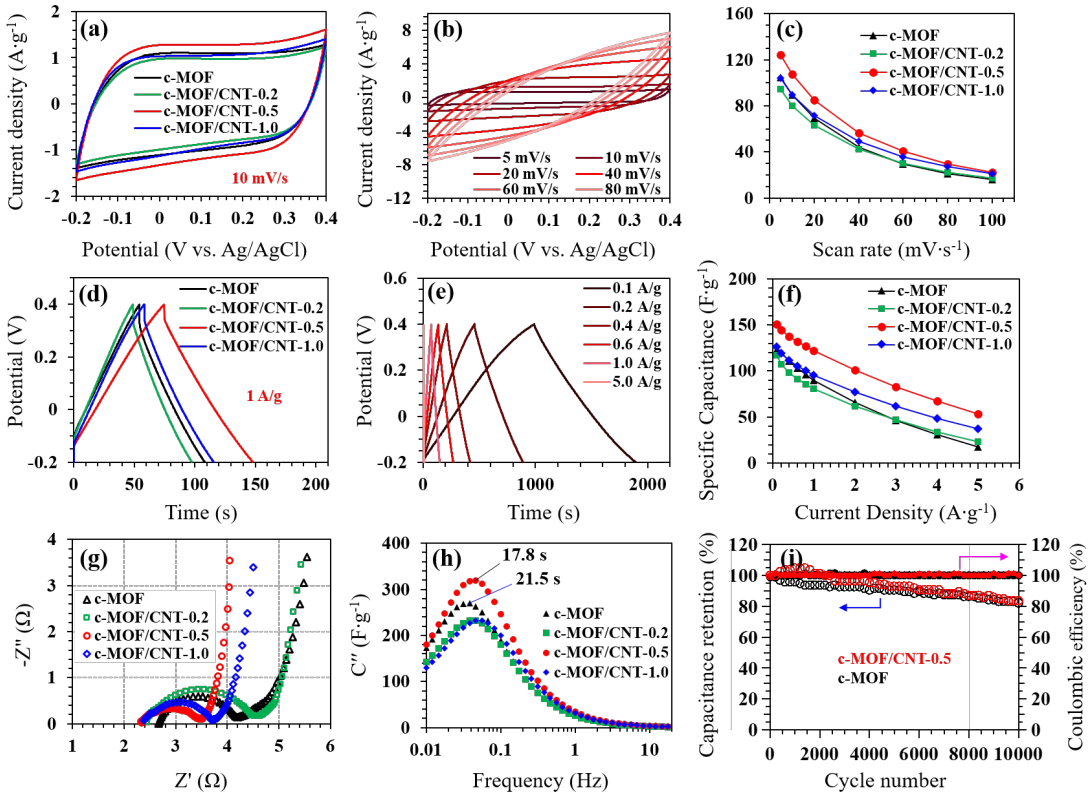

Figure 6. (a) CV curves at a scan rate of 10 $mV \cdot s^{-1}$. (b) CV curves of c-MOF/CNT-0.5 with different scan rates. (c) Specific capacitance at different scan rates. (d) GCD curves at a current density of 1 $A \cdot g^{-1}$. (e) GCD curves of c-MOF/CNT-0.5 in a different current density range of 0.1-5 $A \cdot g^{-1}$. (f) Specific capacitance vs current density. (g) Nyquist plots. (h) Bode plots of imaginary capacitance C" vs frequency. (i) Cycling stability of c-MOF and c-MOF/CNT-0.5 based supercapacitor over 10000 cycles at a current density of 4 $A \cdot g^{-1}$.

To investigate the electrochemical properties of the prepared electrodes, cyclic voltammetry (CV), galvanostatic charge/discharge (GCD), and electrochemical impedance spectroscopy (EIS) measurements were performed under a three-electrode

cell configuration in a neutral aqueous electrolyte (1.0 M Na_2SO_4). As shown in Figure 6a, the electrodes based on c-MOF and c-MOF/CNTs composites show characteristic rectangular CV curves without significant redox peaks, indicating typical double-layer capacitance properties. In addition, the c-MOF/CNT-0.5 electrode exhibits a larger integral area than c-MOF and other c-MOF/CNT composites electrodes, which indicates a higher specific capacity and more electrochemical active sites. Figure 6b shows the CV curves of c-MOF/CNT-0.5 at various scan rates between 5 and 100 $mV \cdot s^{-1}$ in a working potential window of -0.2–0.4 V. The specific capacitance of all electrodes at different scan rates were calculated by Equation (1) are shown in Figure 6c. Thus, the c-MOF/CNT-0.5 electrode has a higher specific capacitance than other electrodes. Also, GCD curves suggested the same situation.

As shown in Figure 6d, the GCD curves of c-MOF and c-MOF/CNT electrodes were symmetrical and linear, indicating excellent electrochemical reversibility. The GCD curves of the c-MOF/CNT-0.5 electrode at various current densities are shown in Figure 6e, which are linear and highly symmetric, and the IR drop is low indicating the excellent stability in the charge/discharge process. As depicted in Figure S8b, the IR drop is lower at a small current density. It increases gradually with increasing current densities. Furthermore, the IR drop of the c-MOF/CNT-0.5 electrode is much lower than that of the other c-MOF/CNT electrode and pristine c-MOF electrodes at the same current density. This means that the overall resistance reduces significantly. The specific capacitances of all electrodes calculated from the GCD curves by Equation (2) are shown in Figure 6f. As the current density increases from 0.1 to 5 $A \cdot g^{-1}$, c-MOF/CNT-0.5 and c-MOF maintain 35% (from 150.7 to 53.3 $F \cdot g^{-1}$) and 14% (from 122.8 to 17.5 $F \cdot g^{-1}$) of their initial capacitances, indicating that c-MOF/CNT-0.5 has a better rate capability than c-MOF. Furthermore, rate capability increases with increasing CNTs content, which can be confirmed by the slop of the curves in Figure S9. The smaller absolute value of the slope indicates the better rate capability.

Electrochemical impedance spectra (EIS) provided helpful information to explain this phenomenon. The Nyquist plots (Figure 6g and Figure S10) of all electrodes

include two regions, an incomplete semicircle obtained in high-frequency areas and a linear tail received in low frequency, respectively. Compared with the other electrodes, c-MOF/CNT-0.5 shows a much smaller charge transfer resistance (R_{ct}), and a more vertical tail means a faster charge transfer and excellent capacitive behavior. To better understand the frequency response of the electrode, the relaxation time constant t_0 was calculated, as shown in Figure 6h. Typically, t_0 represents the minimum time required to discharge the stored energy with 50% efficiency [47]. All c-MOF/CNT electrodes have similar t_0, which was slightly smaller than the value of c-MOF, indicating the faster charge/discharge properties characteristics and the most facile penetration of ions into pores. Cyclic stability results for c-MOF and c-MOF/CNT-0.5 are provided in Figure 6i. Both c-MOF and c-MOF/CNT-0.5 exhibit good cycle stability, retaining above 82% after 10,000 charge/discharge cycles at a current density of 4 $A \cdot g^{-1}$. In conclusion, the addition of CNTs effectively improves the electrochemical properties of c-MOF materials.

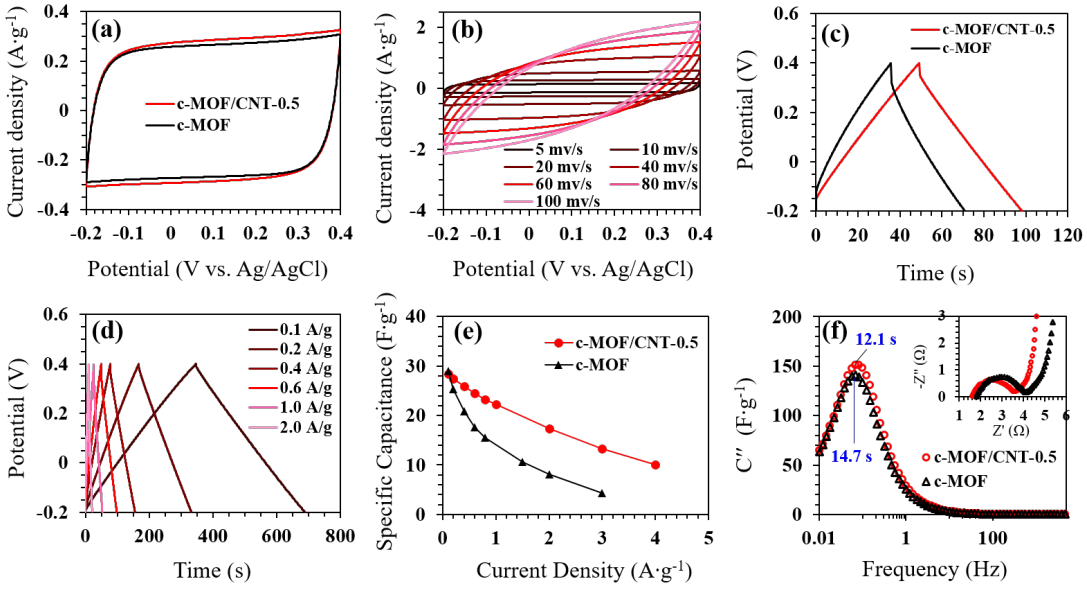

Figure 7. (a) CV curves of the devices at a scan rate of 10 $mV \cdot s^{-1}$. (b) CV curves of c-MOF/CNT-0.5//c-MOF/CNT-0.5 with different scan rates. (c) GCD curves at a current density of 1 $A \cdot g^{-1}$. (d) GCD curves of c-MOF/CNT-0.5//c-MOF/CNT-0.5 with different current densities. (e) Specific capacitance vs current density. (f) Imaginary capacitance C″ vs frequency and Nyquist plots (inset).

To explore the practical application value of c-MOF, c-MOF/CNT-0.5, the symmetric capacitor was assembled with c-MOF, c-MOF/CNT-0.5 as working electrodes in 1.0 M Na_2SO_4 (Figure S11). The CV curves (Figure 7a-b) display an ideal rectangle and a slight deviation with the increasing scan rates (5 to 100 $mV \cdot s^{-1}$). Similarly, the GCD curves (Figure 7c-d) also exhibit a highly symmetrical triangle in 0.1~2 $A \cdot g^{-1}$, reflecting excellent rate performance and fast reaction kinetics. The specific capacitances calculated by GCD discharging time as a function of the current densities are plotted in Figure 7e. The result shows that the specific capacitance of the device is almost one-fourth of that of a single electrode. We can see that the c-MOF/CNT-0.5//c-MOF/CNT-0.5 symmetric capacitor has a higher specific capacitance than the c-MOF//c-MOF symmetric capacitor at current densities from 0.1 to 3 $A \cdot g^{-1}$. As the current density increases from 0.1 to 3 $A \cdot g^{-1}$, c-MOF//c-MOF and c-MOF/CNT-0.5//c-MOF/CNT-0.5 maintain 14.5% (from 29.0 to 4.2 $F \cdot g^{-1}$) and 46.7% (from 28.5 to 13.3 $F \cdot g^{-1}$) of their initial capacitances, indicating that c-MOF/CNT-0.5// c-MOF/CNT-0.5 has a better rate capability than c-MOF//c-MOF.

The relaxation time constant t_0 was plotted for a better comparison of the frequency response of the electrodes (Figure 7f). c-MOF/CNT-0.5//c-MOF/CNT-0.5 device exhibited a short t_0 and a smaller R_{ct} (inset of Figure 7f) than that of c-MOF//c-MOF, revealing that the addition of CNTs had a positive effect on the electro-adsorption/desorption kinetics. Meanwhile, only one peak is observed in Figure 7f, which indicates that there is only one primary charge storage mechanism, which is more likely due to ion adsorption.

4 Conclusions

In summary, we synthesized the composite CNT@c-MOF by directly growing $Ni_3(HITP)_2$ on the CNTs surface and demonstrated the potential application in high-performance supercapacitors in neutral aqueous electrolytes. We identified that CNTs

provide abundant active sites to ensure high capacitance, and $Ni_3(HITP)_2$ nanoarrays that in-situ grow on the surface of CNTs bundles can significantly improve the conductivity and provide enough ion transport pathways. It is confirmed that the c-MOF/CNT-0.5 electrode has higher specific capacitance and better rate capability than that of other c-MOF/CNT electrodes and c-MOF electrodes in both a three-electrode system and aqueous device. In a three-electrode system, the c-MOF/CNT-0.5 electrode has a specific capacitance of 150.7 $F \cdot g^{-1}$ at 0.1 $A \cdot g^{-1}$ in 1 M Na_2SO_4 solution, maintaining 83.5% of the primitive capacitance after 10000 cycles at 4 $A \cdot g^{-1}$. Our results demonstrate that CNT@c-MOF is a promising material platform for addressing the challenge of applying c-MOF into neutral aqueous electrolytes for high-performance electrochemical energy storage applications. We also envisaged that conductive CNT@c-MOF could be a new kind of promising microporous electrode material for other wearable energy storage and gas storage applications.

Acknowledgements

This work was financially supported by the Science and Technology Foundation of Henan Province (No. 192102210044), the National Natural Science Foundation of China (No.U1904171), the Young Backbone Teachers Training Program Foundation of Henan University of Technology, and the Innovative Funds Plan of Henan University of Technology (No. 2020ZKCJ04).

References

[1] Furukawa, H.; Cordova, K. E.; O'Keeffe, M.; Yaghi, O. M. The chemistry and applications of metal-organic frameworks. *Science* **2013**, *341*, 1230444.

[2] Jiao, L.; Wang, Y.; Jiang, H. L.; Xu, Q. Metal-organic frameworks as platforms for catalytic applications. *Adv. Mater.* **2018**, *30*, 1703663.

[3] Zhou, H. C.; Long J. R.; Yaghi, O. M. Introduction to metal-organic frameworks. *Chem. Rev.* **2015**, *112*, 673–674.

[4] Sheberla, D.; Bachman, J. C.; Elias, J. S.; Sun, C. J.; Shao-Horn, Y.; Dincă, M.

Conductive MOF electrodes for stable supercapacitors with high areal capacitance. *Nat. Mater.* **2017**, *16*, 220−224.

[5] Park, J.; Lee, M.; Feng, D.; Huang, Z.; Hinckley, A. C.; Yakovenko, A.; Zou, X.; Cui, Y.; Bao, Z. Stabilization of hexaaminobenzene in a 2D conductive metal−organic framework for high power sodium storage. *J. Am. Chem. Soc.* **2018**, *140*, 10315− 10323.

[6] Shinde, S. S.; Lee, C. H.; Jung, J. Y.; Wagh, N. K.; Kim, S. H.; Kim, D. H.; Lin, C.; Lee, S. U.; Lee, J. H. Unveiling dual-linkage 3D hexaiminobenzene metal-organic frameworks towards long-lasting advanced reversible Zn-Air batteries. *Energy Environ. Sci.* **2019**, *12*, 727−738.

[7] Fan, L.; Hu, Y.; Rao, A. M.; Zhou, J.; Hou, Z.; Wang, C.; Lu, B. Prospects of electrode materials and electrolytes for practical potassium-based batteries. *Small Methods* **2021**, *5*, 2101131.

[8] Miner, E. M.; Fukushima, T.; Sheberla, D.; Sun, L.; Surendranath, Y.; Dincă, M. Electrochemical oxygen reduction catalysed by Ni_3(Hexaiminotriphenylene)$_2$. *Nat. Commun.* **2016**, *7*, 10942.

[9] Downes, C. A.; Clough, A. J.; Chen, K.; Yoo, J. W.; Marinescu, S. C. Evaluation of the H_2 evolving activity of benzenehexathiolate coordination frameworks and the effect of film thickness on H_2 production. *ACS Appl. Mater. Interfaces* **2018**, *10*, 1719−1727.

[10] Yao, M. S.; Lv, X. J.; Fu, Z. H.; Li, W. H.; Deng, W. H.; Wu, G. D.; Xu, G. Layer-by-layer assembled conductive metal−organic framework nanofilms for room-temperature chemiresistive sensing. *Angew. Chem. Int. Ed.* **2017**, *56*, 16510−16514.

[11] Zheng, H.; Zhang, Y.; Liu, L.; Wan, W.; Guo, P.; Nyström, A. M.; Zou, X. One-pot synthesis of metal-organic frameworks with encapsulated target molecules and their applications for controlled drug delivery. *J. Am. Chem. Soc.* **2016**, *138*, 962−968.

[12] Teplensky, M. H.; Fantham, M.; Li, P.; Wang, T. C.; Mehta, J. P.; Young, L. J.; Moghadam, P. Z.; Hupp, J. T.; Farha, O. K.; Kaminski, C. F. et al. Temperature treatment of highly porous zirconium-containing metal-organic frameworks extends drug delivery release. *J. Am. Chem. Soc.* **2017**, *139*, 7522−7532.

[13] Hanikel, N.; Prévot, M. S.; Yaghi, O. M. MOF water harvesters. *Nat. Nanotechnol.*

2020, *15*, 348–355.

[14] Kim, H.; Rao, S. R.; Kapustin, E. A.; Zhao, L.; Yang, S.; Yaghi, O. M.; Wang, E. N. Adsorption-based atmospheric water harvesting device for arid climates. *Nat. Commun.* **2018**, *9*, 1191.

[15] Fathieh, F.; Kalmutzki, M. J.; Kapustin, E. A.; Waller, P. J.; Yang, J.; Yaghi, O. M. Practical water production from desert air. *Sci. Adv*. **2018**, *4*, eaat3198.

[16] Guo, M.; Wang, J.; Dou, H.; Gao, G.; Wang, S.; Wang, J.; Xiao, Z.; Wu, G.; Yang, X.; Ma, Z. F. Agglomeration-resistant 2D nanoflakes configured with super electronic networks for extraordinary fast and stable sodium-ion storage. *Nano Energy* **2019**, *56*, 502–511.

[17] Mulzer, C. R.; Shen, L.; Bisbey, R. P.; McKone, J. R.; Zhang, N.; Abruña, H. D. Superior charge storage and power density of a conducting polymer-modified covalent organic framework. *ACS Central Sci.* **2016**, *2*, 667–673.

[18] Ramachandran, R.; Xuan, W.; Zhao, C.; Leng, X.; Sun, D.; Luo, D.; Wang, F. Enhanced electrochemical properties of cerium metal-organic framework based composite electrodes for high-performance supercapacitor application. *RSC Adv.* **2018**, *8*, 3462–3469.

[19] Givaja, G.; Amo-Ochoa, P.; Gómez-García, C. J.; Zamora, F. Electrical conductive coordination polymers. *Chem. Soc. Rev.* **2011**, *41*, 115–147.

[20] Hosseininan, A.; Amjad, A.; Khanmiri, R. H.; Kalhor, E. G.; Babazadeh, M.; Vessally, E. Nanocomposite of ZIF-67 metal-organic framework with reduced graphene oxide nanosheets for high-performance supercapacitor applications. *J. Mater. Sci. Mater. Electron.* **2017**, *28*, 18040–18048.

[21] Wen, P.; Gong, P.; Sun, J.; Wang, J.; Yang, S. Design and synthesis of Ni-MOF/CNT composites and rGO/carbon nitride composites for an asymmetric supercapacitor with high energy and power density. *J. Mater. Chem. A* **2015**, *3*, 13874-13883.

[22] Takaishi, S.; Hosoda, M.; Kajiwara, T.; Miyasaka, H.; Yamashita, M.; Nakanishi, Y.; Kitagawa, Y.; Yamaguchi, K.; Kobayashi, A.; Kitagawa, H. Electroconductive porous coordination polymer $Cu[Cu(pdt)_2]$ composed of donor and acceptor building

units. *Inorg. Chem.* **2009**, *48*, 9048–9050.

[23] Gándara, F.; Uribe-Romo, F. J.; Britt, D. K.; Furukawa, H.; Lei, L.; Cheng, R.; Duan, X.; O'Keeffe, M.; Yaghi, O. M. Porous, Conductive metal-triazolates and their structural elucidation by the charge-flipping method. *Chem.-Eur. J.* **2012**, *18*, 10595–10601.

[24] Talin, A. A.; Centrone, A.; Ford, A. C.; Foster, M. E.; Stavila, V.; Haney, P.; Kinney, R. A.; Szalai, V.; EI Gabaly, F.; Yoon, H. P. et al. Tunable electrical conductivity in metal-organic framework thin-film devices. *Science* **2014**, *343*, 66–69.

[25] Sun, L.; Hendon, C. H.; Minier, M. A.; Walsh, A.; Dincă, M. Million-fold electrical conductivity enhancement in Fe_2(DEBDC) versus Mn_2(DEBDC) (E = S, O). *J. Am. Chem. Soc.* 2015, *137*, 6164–6167.

[26] Zheng, Y.; Zheng, S.; Xua, Y.; Xue, H.; Liu, C.; Pang, H. Ultrathin two-dimensional cobalt-organic frameworks nanosheets for electrochemical energy storage. *Chem. Eng. J.* **2019**, *373*, 1319–1328.

[27] Park, S. S.; Hontz, E. R.; Sun, L.; Hendon, C. H.; Walsh, A.; Van Voorhis, T.; Dincă, M. Cation-dependent intrinsic electrical conductivity in isostructural tetrathiafulvalene-based microporous metal-organic frameworks. *J. Am. Chem. Soc.* **2015**, *137*, 1774–1777.

[28] Campbell, M. G.; Sheberla, D.; Liu, S. F.; Swager, T. M.; Dincă, M. Cu_3(hexaiminotriphenylene)$_2$: an electrically conductive 2D metal-organic framework for chemiresistive sensing. *Angew. Chem. Int. Edit.* **2015**, *54*, 1–5.

[29] Skorupskii, G.; Dincă, M. Electrical conductivity in a porous, cubic rare-earth catecholate. *J. Am. Chem. Soc.* **2020**, *142*, 6920–6924.

[30] Chen, T.; Dou, J. H.; Yang, L.; Sun, C.; Libretto, N. J.; Skorupskii, G.; Miller, J. T.; Dincă, M. Continuous electrical conductivity variation in M_3(Hexaiminotriphenylene)$_2$ (M = Co, Ni, Cu) MOF alloys. *J. Am. Chem. Soc.* **2020**, *142*, 12367–12373.

[31] Cai, D.; Lu, M.; Li, L.; Cao, J.; Chen, D.; Tu, H.; Li, J.; Han, W. A highly conductive MOFs of graphene analogue Ni_3(HITP)$_2$ as a sulfur host for high-performance lithium-sulfur batteries. *Small* **2019**, *15*, 1902605.

[32] Feng, D.; Lei, T.; Lukatskaya, M. R.; Park, J.; Huang, Z.; Lee, M.; Shaw, L.; Chen, S.; Yakovenko, A. A.; Kulkarni, A. et al. Robust and conductive two-dimensional metal-organic frameworks with exceptionally high volumetric and areal capacitance. *Nat. Energy* **2018**, *3*, 30–36.

[33] Dou, J.; Arguilla, M. Q.; Luo, Y.; Li, J.; Zhang, W.; Sun, L.; Mancuso, J. L.; Yang, L.; Chen, T.; Parent, L. R. et al. Atomically precise single-crystal structures of electrically conducting 2D metal-organic frameworks. *Nat. Mater.* **2021**, *20*, 222–228.

[34] Gutzler, R.; Perepichka, D. F. π-Electron conjugation in two dimensions. *J. Am. Chem. Soc.* **2013**, 135, 16585–16594.

[35] Sheberla, D.; Sun, L.; Blood-Forsythe, M. A.; Er, S.; Wade, C. R.; Brozek, C. K.; Aspuru-Guzik, A.; Dincă, M. High electrical conductivity in Ni_3(2,3,6,7,10,11-hexaiminotriphenylene)$_2$, a semiconducting metal−organic graphene analogue. *J. Am. Chem. Soc.* **2014**, *136*, 8859−8862.

[36] Foster, M. E.; Sohlberg, K.; Allendorf, M. D.; Alec Talin, A. Unraveling the semiconducting/metallic discrepancy in $Ni_3(HITP)_2$. *J. Phys. Chem. Lett.* **2018**, *9*, 481–486.

[37] Xie, L. S.; Skorupskii, G.; Dincă, M. Electrically conductive metal-organic frameworks. *Chem. Rev.* **2020**, *120*, 16, 8536–8580.

[38] Lu, M.; Liu, S.; Chen, J.; Zhang, X.; Zhang, J.; Li Z.; Hou, B. Rational-designed hybrid aerogels for ultra-flyweight electrochemical energy storage. *J. Phys. Chem. C* **2020**, 124, 15688–15697.

[39] Ding, H.; Zhou, J.; Rao, A. M.; Lu, B. Cell-like-carbon-micro-spheres for robust potassium anode. *Natl Sci Rev*, **2021**, *8*, nwaa276.

[40] Venkataraman, A.; Amadi, E. V.; Chen Y.; Papadopoulos, C. Carbon nanotube assembly and integration for applications. *Nanoscale Res. Lett.* **2019**, *14*, 220.

[41] Ansari, S. N.; Saraf, M.; Gupta, A. K.; Mobin, S. M. Functionalized Cu-MOF@CNT hybrid: synthesis, crystal structure and applicability in supercapacitors. *Chem. Asian J.* **2019**, *14*, 3566–3571.

[42] Shen, C. H.; Chuang, C. H.; Gu, Y. J.; Ho, W. H.; Song, Y. D.; Chen, Y. C.; Wang, Y. C.; Kung, C. W. Cerium-based metal−organic framework nanocrystals

interconnected by carbon nanotubes for boosting electrochemical capacitor performance. *ACS Appl. Mater. Interfaces* **2021**, *13*, 16418−16426.

[43] Sreekanth, T. V. M.; Dillip, G. R.; Nagajyothi, P. C.; Yoo, K.; Kim, J. Integration of marigold 3D flower-like Ni-MOF self-assembled on MWCNTs via microwave irradiation for high-performance electrocatalytic alcohol oxidation and oxygen evolution reactions. *Applied Catalysis B: Environmental* **2021**, *285*, 119793.

[44] Lu, M.; Wang, G.; Li, B.; Chen, J.; Zhang, J.; Li, Z.; Hou, B. Molecular interaction balanced one- and two-dimensional hybrid nanoarchitectures for high-performance supercapacitors. *Phys. Chem. Chem. Phys.* **2019**, *21*, 22283– 22292.

[45] Chen, S.; Dai, J.; Zeng, X. C. Metal–organic kagome lattices M_3(2,3,6,7,10,11-hexaiminotriphenylene)$_2$ (M = Ni and Cu): from semiconducting to metallic by metal substitution. *Phys. Chem. Chem. Phys.* **2015**, *17*, 5954–5958.

[46] Miner, E. M.; Fukushima, T.; Sheberla, D.; Sun, L.; Surendranath, Y.; Dincă, M. Electrochemical oxygen reduction catalysed by Ni_3(hexaiminotriphenylene)$_2$. *Nat. Commun.* **2016**, *7*, 10942.

[47] Taberna, P. L.; Simon, P.; Fauvarque, J. F. Electrochemical characteristics and impedance spectroscopy studies of carbon-carbon supercapacitors. *J. Electrochem, Soc.* **2003**, *150*, A292–A300.

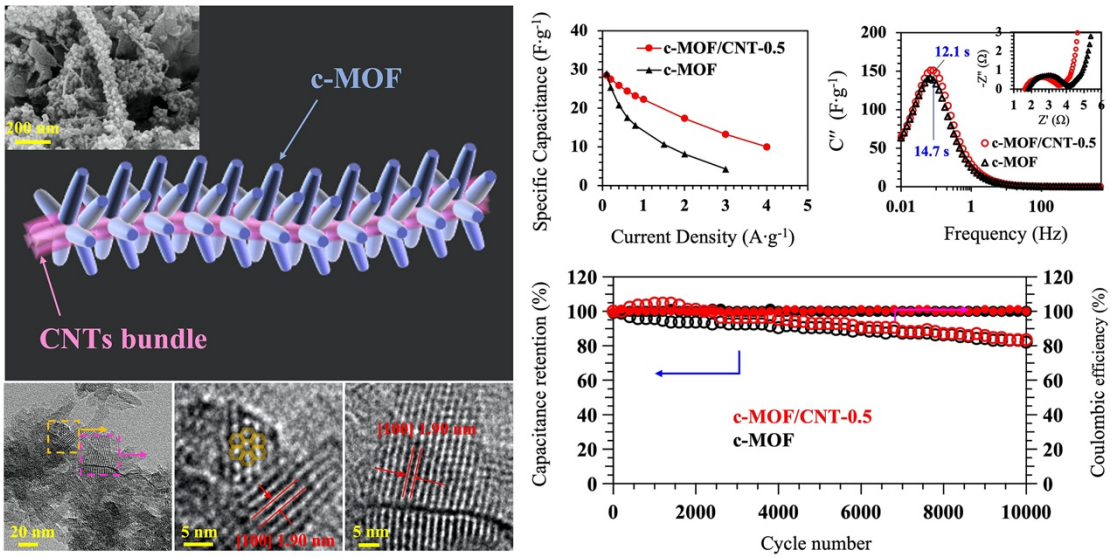

A new synthesis approach for fabricating carbon nanotubes (CNTs) and conductive metal-organic frameworks (c-MOF) core-shell structures (CNT@MOFs) has been proposed, which enables c-MOF based supercapacitors in neutral aqueous electrolytes with a record energy storage performance beyond previously reported works.

Supporting Information

In situ Growth CNT@MOFs Core-Shell Structures Enabling High Specific Supercapacitances in Neutral Aqueous Electrolyte

*Mingxia Lu[a], Gang Wang[a,]**, Xiping Yang[a], and Bo Hou[b,]**

[a] School of Chemistry and Chemical Engineering, Henan University of Technology, Zhengzhou 450001, P. R. China.

[b] Department of Physics and Astronomy, Cardiff University, Cardiff CF24 3AA, UK

* Corresponding author: Email: HouB6@cardiff.ac.uk (Bo Hou)

** Corresponding author: Email: gwang198@gmail.com (Gang Wang)

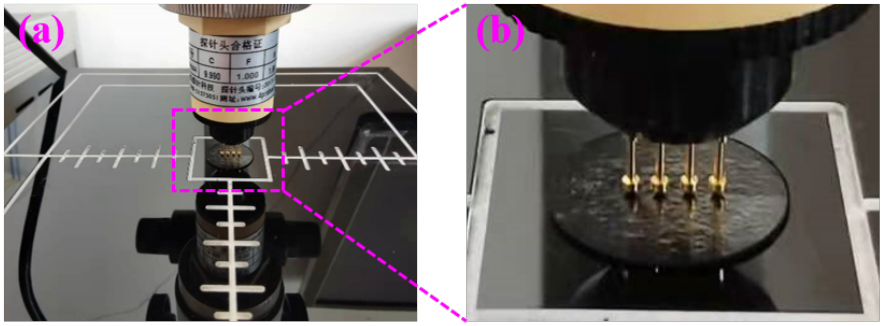

(c) samples	Electronic conductivity ($S \cdot cm^{-1}$)
c-MOF	5
c-MOF/CNT-0.2	5.667
c-MOF/CNT-0.5	6.250
c-MOF/CNT-1.0	7.429
c-MOF/CNT-2.0	10
c-MOF/CNT-3.0	12.5

Figure S1. (a-b) Determination of electronic conductivity by four-point probes method. (c) The electronic conductivity of all samples.

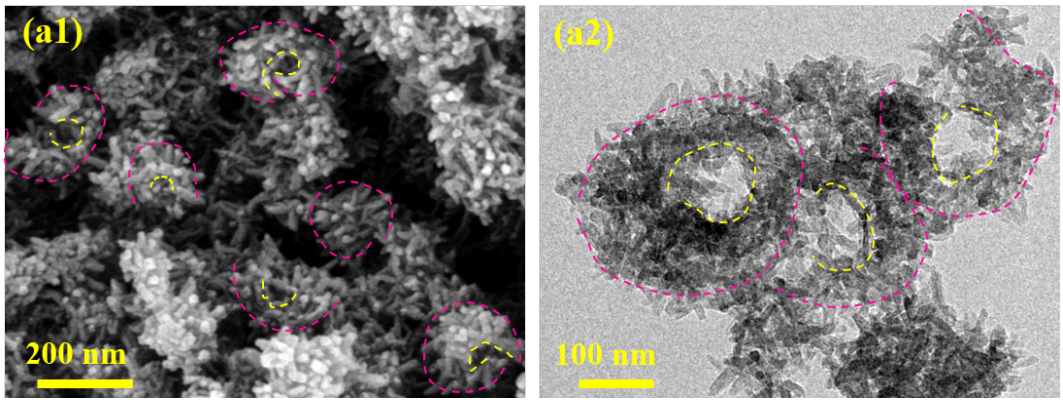

Figure S2. (a) SEM images of c-MOF. (b) TEM images of c-MOF.

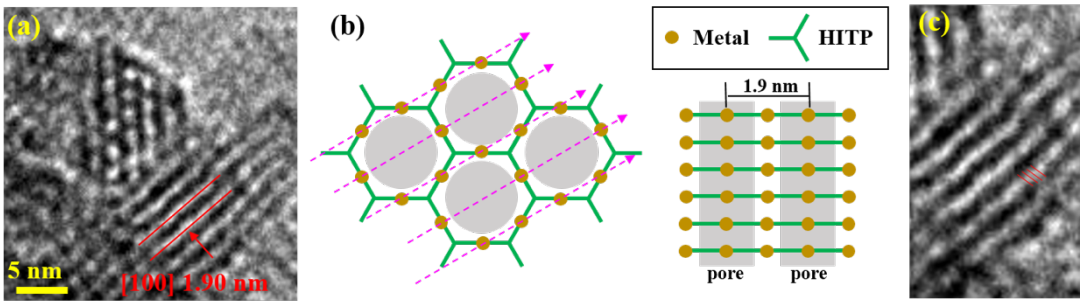

Figure S3. (a) TEM images of rods of $Ni_3(HITP)_2$ with diameters about 12 nm. Well-aligned fringes indicate the ordered 1D pore structure of $Ni_3(HITP)_2$. (b) Left: schematic representation of one layer of $Ni_3(HITP)_2$ and the pore arrangement that observed under TEM. Right: schematic representation of a stacking configuration of six layers of $Ni_3(HITP)_2$ parallel to 2D layers. Pink dashed arrows in the left scheme indicate the direction of viewing for the right scheme. (c) Interlayer π-stacking of layers of $Ni_3(HITP)_2$ (red lines).

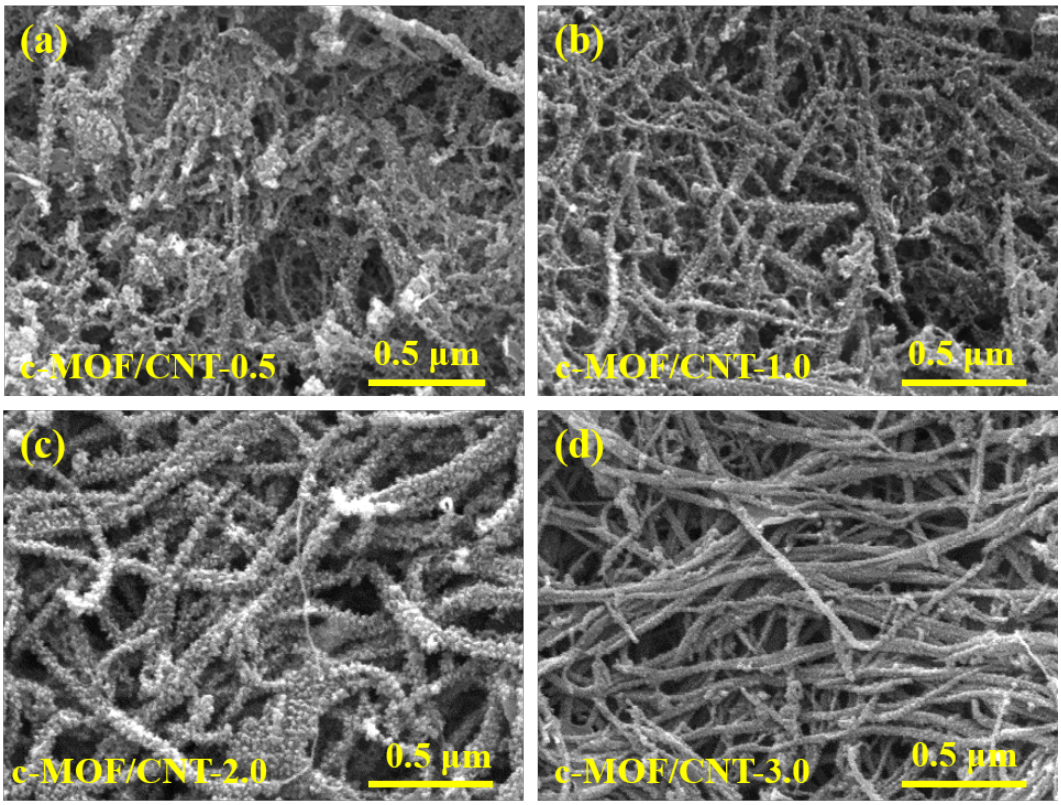

Figure S4. SEM images of (a) c-MOF/CNT-0.5, (b) c-MOF/CNT-1.0, (c) c-MOF/CNT-2.0, (d) c-MOF/CNT-3.0.

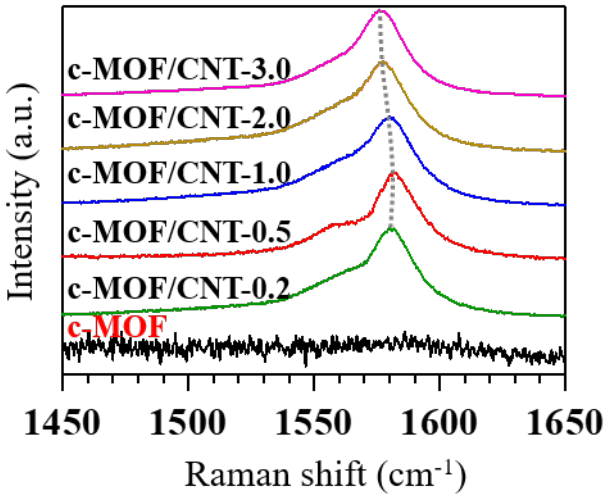

Figure S5. Raman spectra of all samples.

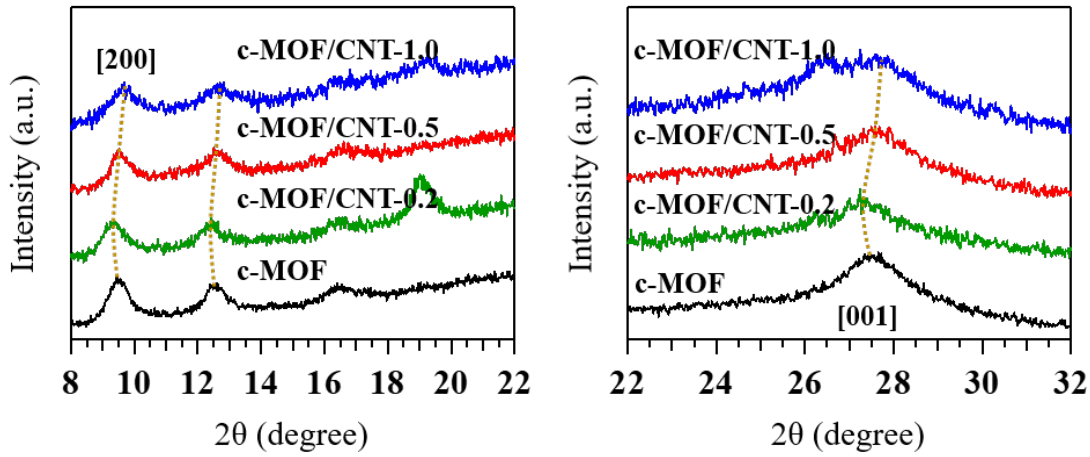

Figure S6. XRD pattern at different regions.

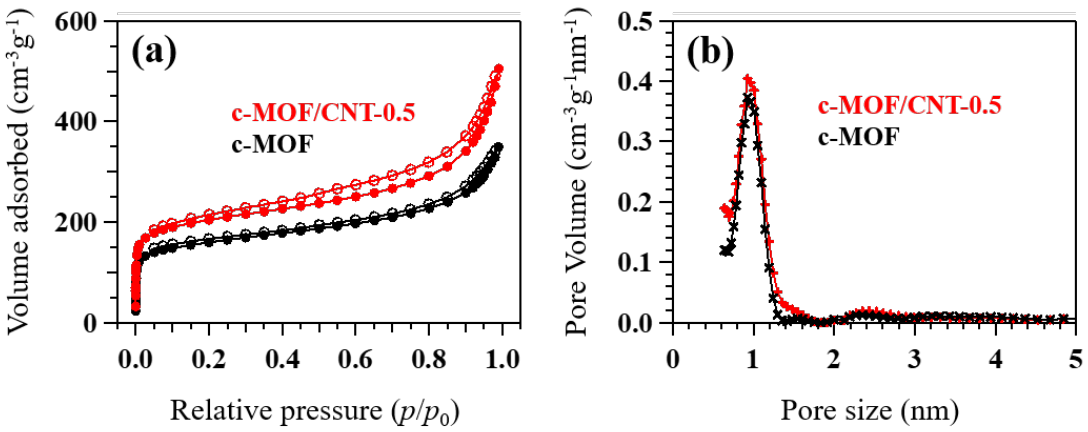

Figure S7. (a) N_2 adsorption and desorption isotherms at 77 K. (b) Pore size distribution[1].

Table S1. Pore structure parameters of MOF and MOF/CNT-0.5.

samples	$S_{BET}/(m^2 \cdot g^{-1})$[a]	$V_{Tot}/(m^3 \cdot g^{-1})$[b]	$V_{Mic}/(m^3 \cdot g^{-1})$[c]
c-MOF	589.09	0.541	0.158
c-MOF/CNT-0.5	753.22	0.783	0.210

[a] Surface area ($m^2 \cdot g^{-1}$) calculated from nitrogen adsorption based on the BET model.
[b] Total pore volume ($m^2 \cdot g^{-1}$) calculated at $p/p_0 = 0.989$.
[c] Micropore volume ($m^2 \cdot g^{-1}$)

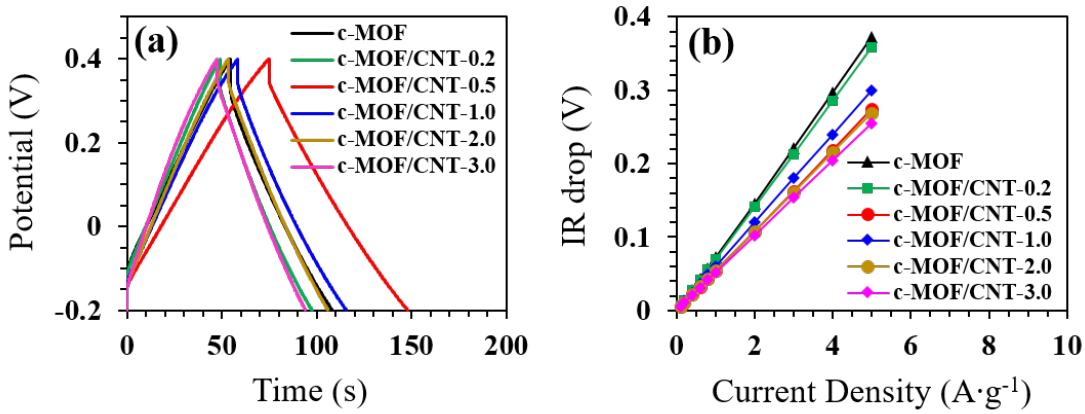

Figure S8. (a) GCD curves of all samples at a current density of 1 $A \cdot g^{-1}$. (b) IR drop vs current density.

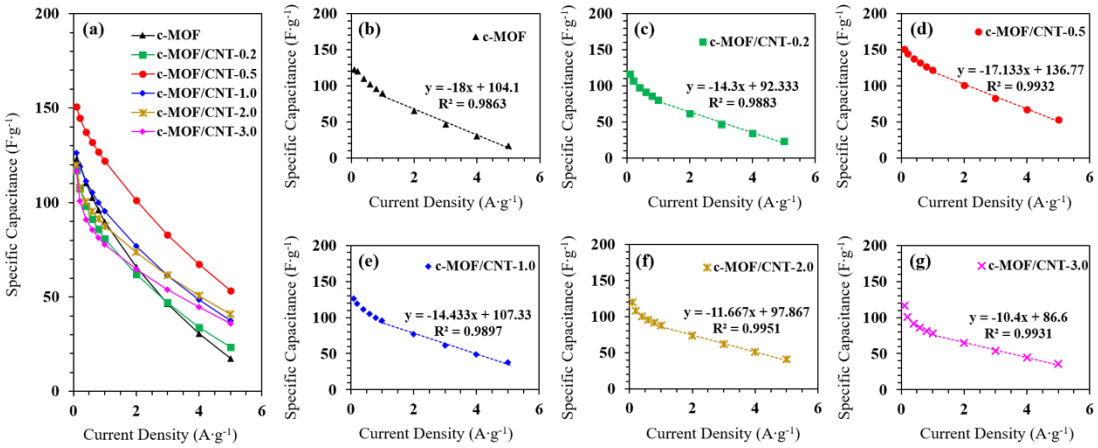

Figure S9. (a) Specific capacitance versus current density. (b-g) The rate capability (the slop of the curves) changes with the CNTs content.

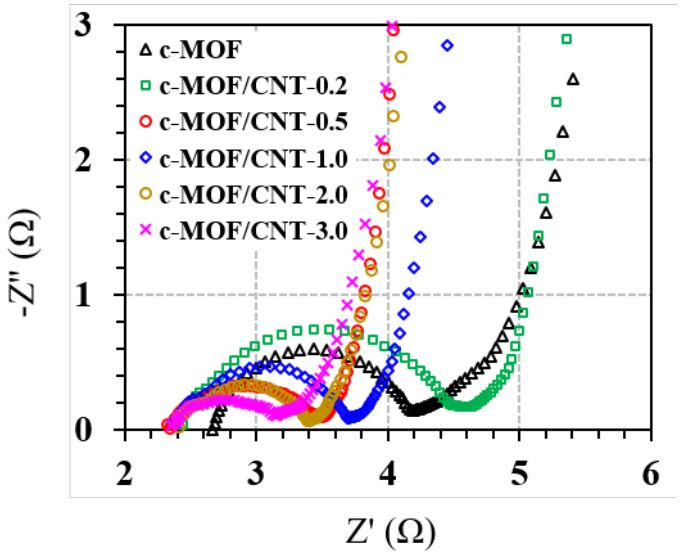

Figure S10. Nyquist plots of all samples.

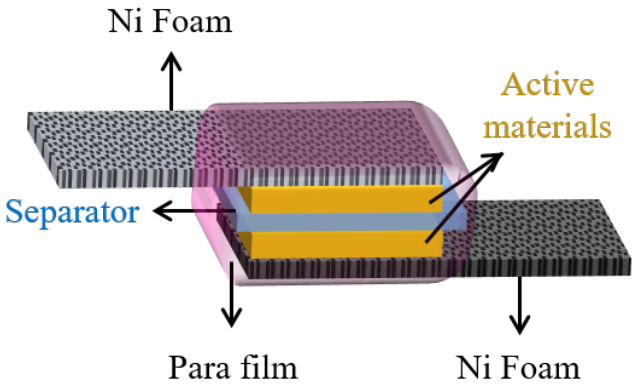

Figure S11. Schematic illustration of the as-prepared symmetrical supercapacitor configuration.

Reference

[1] Ravikovitch, P. I.; Haller, G. L.; Neimark, A. V. Density functional theory model for calculating pore size distributions: pore structure of nanoporous catalysts. Advances in Colloid and Interface Science. **1998**, *76–77*, 203-226.